BIOINSPIRED HIERARCHICAL CERAMIC SUTURES FOR MULTI-MODAL PERFORMANCE

Z. Katz*, H. Yazdani Sarvestani[1], J. Gholipour[1], and B. Ashrafi[1]
[1] Aerospace Manufacturing Technology Center, National Research Council, 5145 Decelles Avenue,
Montreal, QC H3T 2B2 Canada
* Corresponding author (zachary.katz@mail.mcgill.ca)

Keywords: *Toughness, biomimicry, laser processing*

ABSTRACT

Natural suture structures, characterized by hard segments joined along a patterned weak interface, have been found to provide unique toughening mechanisms to otherwise brittle bulk biological materials. Using a biomimetic approach, a hierarchical ceramic suture inspired by the sutures of white-tailed deer crania and diabolical ironclad beetle exoskeletons was developed. Overlapping geometries unlocked twin energy absorption mechanisms. Ceramic panels with Surlyn®-infiltrated precision laser-cuts were fabricated using a semi-automated smart advanced manufacturing platform. A parametric study consisting of four-point bending, fracture toughness, and tensile tests evaluating toughness, strength, and stiffness with geometrical interlocking at two hierarchical orders was conducted. Digital image correlation was utilized in order to analyze local toughening mechanisms and characterize failure modes in the fracture tests. In all three metrics, panels with a second order of hierarchy outperformed the anti-trapezoidal equivalents. One geometry in particular flexed to over 80% strain before failing, offering twice the toughness of the baseline. The high order of fractal interlocking at multiple scales and overlapping teeth were found to provide high flexibility and failure resistance while progressive fracture mechanisms delayed catastrophic failure by up to 50%.

1. Methods and Materials

1.1. Design

In order to develop an easily variable cut program, Solidworks (Dassault Systems) was used to create a parametrically defined interface. The hierarchical teeth are a combination of anti-trapezoidal teeth at *N1*, having a 14 mm amplitude, and tangentially constrained ellipses with an aspect ratio of 1.8:1 and amplitude of 2.6 mm at *N2* (inspired by the diabolical iron clad beetle [1]). The amplitudes were chosen such that two samples could fit within a 114.3 mm wide square panel with a minimum of three full interlocking teeth per horizontal edge per length scale. Furthermore, a 1:1 *N1* tooth aspect ratio was used in order to fit four *N2* teeth on the anti-trapezoidal interlocking interface, resulting in 180° rotational symmetry. Therefore, the samples are denoted as the θ_1-θ_2 (*N2*) design where θ_1 (*N1*) is equal to 5°, 15°, or 25° whereas θ_2 (*N2*) equals 5°, 15°, 25°, or 35°. Amplitudes (A_1 and A_2) and interlocking angles (θ_1 and θ_2) at both length scales were used to define the geometry, with interlocking angles serving as the variable parameters (see Fig. 1). The 1.5-tooth unit cells of each geometry were exported in *dxf* file format to be imported directly into IPGWeld processing software and repeated to create the 3-tooth suture.

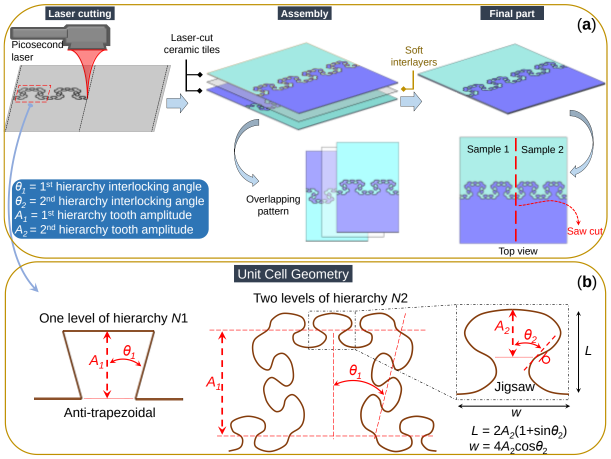

Figure 1: (**a**) Design and manufacturing steps of the multilayered ceramic sutures: laser machining ceramic tiles and simplified lamination, and (**b**) Design and arrangement of material architectures: anti-trapezoidal and jigsaw.

1.2. Experimental Tests Configurations

1.2.1. Four-point bending tests

Four-point bending samples 55.0 mm in width, 114.3 mm in height, and 1.6 mm in thickness were manufactured of overlapping alumina tiles with interlocked suture geometries composing of three full teeth plus two half teeth. The samples feature a weak interface composed of the thermoplastic Surlyn®. Fifteen double-layer panels (*N1-N2* sutures), including *N1* suture samples as a baseline (see Fig. 2), were tested in flexure loosely adapted from ASTM Standard C1161-18. The bending fixture's outer span was set to 80 mm and inner span to 40 mm. Loading rate was set at 0.2 mm/min with data acquisition occurring at a rate of 10 Hz in order to clearly capture the progressive failure of the samples. The width and thickness of each sample were measured in three locations and averaged to provide sample dimensions. Data analysis was carried out using Python 3. Flexural stress for a sample whose inner span is half its outer span is computed using Eq. (1):

$$\sigma = \frac{3FL}{4bd^2} \tag{1}$$

where *F* is load, *L* is the outer support span, *b* is sample width, and *d* is sample thickness. The ultimate flexural strength was extracted from the maximum of each stress-strain curve. Stiffness was computed by taking slope of the curve for the first 100 seconds (linear region, before any fracture) using linear regression *scipy* module in Python 3. Toughness was calculated using Python *numpy* trapezoidal rule. All analysis methods were previously validated to agree with manual analysis.

1.2.2. Fracture toughness testing

All samples were tested in fracture toughness performance loosely based on the ASTM-E399-20a, standard for linear-elastic plane-strain for metallic materials. The standard recommends a crack length to sample width ratio of greater than 0.2, however, a crack of length 8 mm with a minimum cut length (caused by circular blade cutting at an angle) being 6.2 ± 0.1 mm. The notch was cut with a Struers circular cut off wheel equipped with a diamond saw blade with a thickness of 0.6 mm. A crack length of 8 mm gives a length to sample width ratio of 0.14, (0.008m/0.057m). While this is outside the acceptable range for a representative test, we compared all samples with this value and assumed this difference in ratio to be remained valid.

Samples identical to those tested in bending were notched using a Struers circular cut off wheel equipped with a diamond saw blade (M0D31, Struers, Denmark) with a thickness of 0.6 mm. The notching distance has the consequent minimum cut length (caused by circular blade cutting at an angle) being 6.2 ± 0.1 mm. Green painter's tape was then wrapped around the top and bottom of the samples six times in order to counteract localized compression in the grips causing premature fracture at the grip site (serrated, 25×25 mm^2). The pneumatic grips (MTS Systems Advantage 2 kN Pneumatic Grip) were mounted to a MTS 50 kN load frame (810 Material Test System) using custom machined adapters. The setup is self-aligning under tension so ensuring rotational alignment. The pneumatic grips initially gripped the samples at 207 kN before increasing the pressure to 345 kN (25 mm^2 grips, 215 N of grip force). Prior to testing, the samples were sprayed with a speckled black dot pattern for the digital image correlation (DIC) to track localized deformations, with image acquisition occurring at 2 Hz. The extension rate was set to 5 mm/min and the samples were loaded until failure, defined as edge to edge crack propagation.

By ASTM E399, method A4 (compact specimens) was adapted for our application. Fracture toughness (K) is calculated using Eq. (2):

$$K = \frac{P}{B\sqrt{W}} \times f\left(\frac{a}{W}\right) \tag{2}$$

where P is the critical load, B is the specimen thickness, W is the specimen width, and a the notch length, and $f(a/W)$ is:

$$f\left(\frac{a}{W}\right) = \frac{\left(2+\frac{a}{W}\right)\left[0.886+4.64\left(\frac{a}{W}\right)-13.32\left(\frac{a}{W}\right)^2+14.72\left(\frac{a}{W}\right)^3-5.6\left(\frac{a}{W}\right)^4\right]}{\left(1-\frac{a}{W}\right)^{\frac{3}{2}}} \tag{3}$$

Accurate within 0.5% for a/W ratios ranging from 0.2 to 1, with the tested samples having a/W = 0.1, thus assumed to be within reasonable accuracy limits.

1.2.3. Tensile testing

Blank dogbone samples of varying geometries were tested using a custom fixture to find a geometry that would lead to failure in the gauge region. The dogbones had to be laser cut from standard 114.30 mm square panels, which served as the major limitation for the design. It was consequently decided to use a 2 tooth (vs. 4 tooth) design to achieve a narrow enough gauge region such that samples would reliably fail in the gauge. The same MTS tensile testing machine used for fracture testing was used for tensile testing, with a 10 kN load cell installed in order to capture any progressive failure, which otherwise could be hidden by excessive noise caused by the hydraulic grips. Further, a laser extensometer (2710-11T, Applied Tests Systems, Inc., USA) was used, as the reflective tape was able to be put directly on the fixture for reliable strain results. Stress was calculated as $\frac{P}{bw}$, while strain was calculated as $\frac{l-l_0}{l_0}$. Ultimate tensile strength was taken as the critical stress while the slope of the first 500 data points of the stress strain curve were used to calculate the stiffness. Toughness was calculated using numpy's trapezoidal rule in python, taking the area under the stress-strain curve.

1.3. Digital Image Correlation (DIC)

A 3D DIC system was used during the tensile tests to measure the deformation of the ceramics (see Fig. 4). The stereoscopic DIC system consisted of two high-speed cameras (Trilion Aramis Adjustable (2D) using GOM Image processing), set to capture images at two frames per second (fps) with a resolution of 12 megapixels (4096×3000 pixels). A stochastic speckle pattern was sprayed on the surface of the ceramic using a black paint canister. The double-layer ceramic tile provided a natural white coloured background, hence the maximum grayscale contrast can be achieved using black paint or ink. DIC data was analyzed using GOM Aramis version 6.3. Through determining the correspondence between each of the deformed and reference subsets (regularized square regions) the full field displacement over the area of the interest can be calculated and then later differentiated to produce a full field strain map for each of the test images. However, due to significant crack nucleation and propagation throughout the area of interest during the tests, the strain data maps experience artifacts along and around the crack path as the cracked region results in fictitious strain. Thus, the strain data were only used for qualitative purposes to capture the failure initiation and propagation throughout the specimens, while the displacement data was used for quantitative comparisons and analysis.

1.4. Data Analysis Methods

Fracture testing data was cleaned using a low-pass filter implemented in python to counteract noise generated by the 50 kN load cell. Adjustments were made to the testing apparatus to reduce noise, eliminating the need for post processing on the tensile data. As the tensile samples were constrained in a fixture rather than directly gripped, the 10 kN load cell could be placed below the hydraulic grips of the apparatus, the major source of noise.

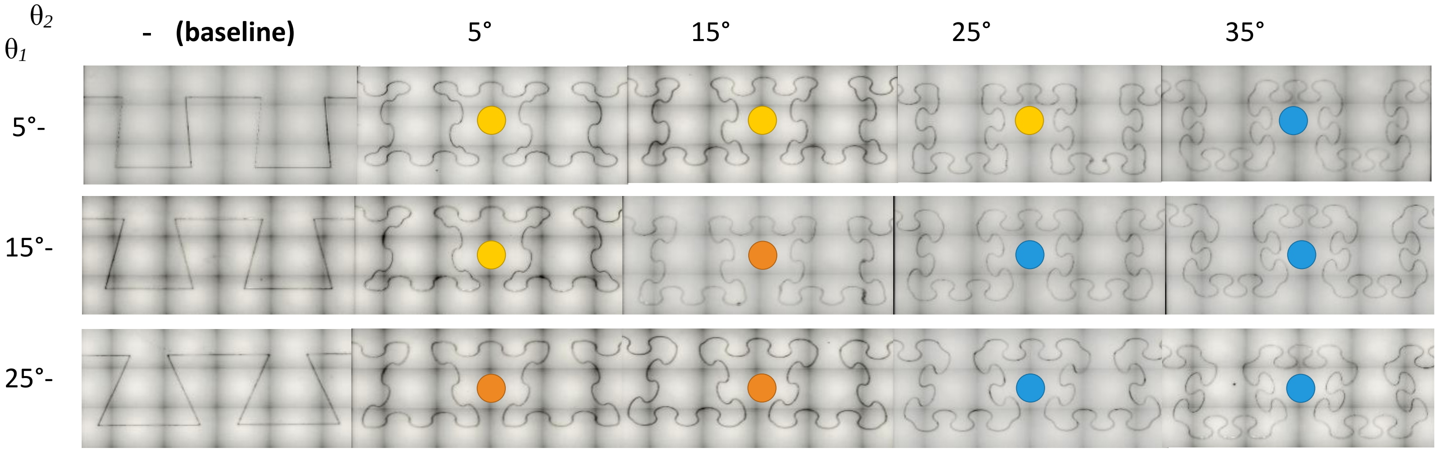

Figure 2: Microscopy images of the samples where the *y*-axis corresponds to *N1* interlocking angle, and the *x*-axis corresponds to the *N2* interlocking angle (the scale is 500 µm, *Colours classify 3 types of corner teeth).

2. Results

2.1. Tensile

Tensile strength, stiffness, and toughness were evaluated through uniaxial loading as shown in Fig. 4. Each sample demonstrated comparable failure mechanisms, except for the 15°-25° sample, which exhibited a large progressive failure characteristic of failure of one side of the laminate. Looking closely at the force-displacement curves, small drops in stress can be observed attributed to progressive failure for most samples, clearly illustrated by the 25°-5° and 25°-35° samples. Unlike the bending samples, the progressive failure does not significantly decrease strength. The stress-strain curves also illustrate stiffening of the samples with increasing strain (see Fig. S1). The samples exhibiting only *N1* suture geometry was among the least stiff and least strong, just like the other loading modes.

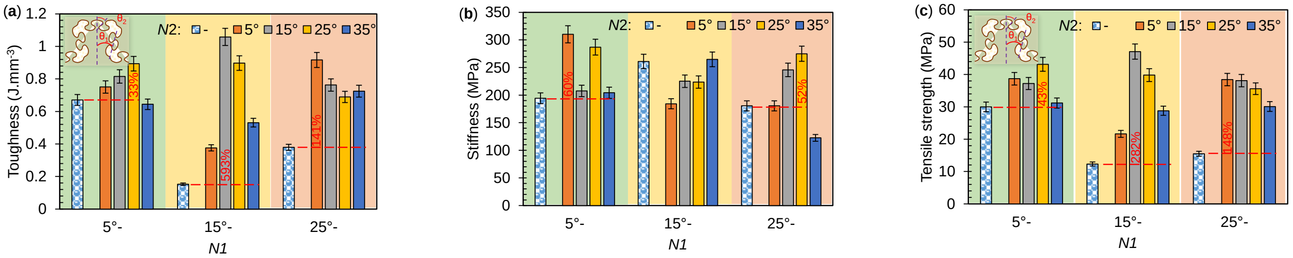

Figure 3: Tensile properties of the ceramic sutures: (**a**) Energy absorption, (**b**) Stiffness and (**c**) Tensile strength.

In tensile, the 5°-5° and 5°-25° samples were the stiffest, exhibiting 60% and 50% greater stiffness than the *N1* sample, respectively, as seen in Fig. 3b. The 15°- sample exhibited relatively high stiffness, beating out many of the *N2* samples. However, the 15°-35° sample is still stiffer. There does appear to be a potential correlation between *N2* interlocking angle and stiffness, particularly for *N1* of 15°- and 25°- , however for the 25°- sample there is an optimal stiffness before it drops off. Improvements in ultimate tensile strength exhibited for all three geometry groups (*N1*-*N2* sutures where *N1*: 5°, 15°, 25° and *N2*: 5°, 15°, 25°, 35°) over the baselines (i.e., *N1* sutures). While the 5°- sample did exhibit greater strength than some of the hierarchical samples, it was beat out by all 5°-hierarchical samples in its category. For the 5°- sutures, no real trend is observed, however the 15°-sutures show a peak at *N2*: 15°, while the 25°- samples show increasing strength with decreasing *N2* interlocking angle. The 15°-15° sample exhibited the greatest tensile strength (caused by teeth fracture and material damage or teeth pullout), with a 280% improvement over the 15°- sample. The 5°-25° sample, competing with the relatively high performing 5°-sample, still offered an increase in strength by 40%. Toughness is increasing with *N2* interlocking angle for the 5°-sample, up until 5°-25° where it decreased. Similarly, the 15°- set showed a peak at 15°-15°, the absolute toughest sample with a seven-fold increase over the *N1* only sample. The 25°- set showed a general decrease in toughness with *N2* interlocking, following the trend of decreased properties with increasing *N2* interlocking for this set. The 5°- suture exhibited impressive toughness, beating out even the 5°-35° suture, however generally introducing geometric hierarchy improved the toughness of a sample as shown in Fig. 3a. Even the 25°-5° sample offered 141% improvements over the 25°- sample. The 5°- samples exhibited a nearly linear increase in toughness up to their maximum at 5°-25°.

2.2. *Four-point Bending*

In order to evaluate the impact of suture geometry on strength, stiffness, and toughness, fifteen suture samples were tested in a flexure condition. Figure 5 presents the bending properties of the ceramic sutures. The samples exhibiting only one order of hierarchy, e.g. “5°-“, performed worse in terms of both strength and flexibility than all *N2* samples with two orders of hierarchy. The 5°- sample exhibits sudden, catastrophic failure, whereas the 15°- and 25°- sample exhibit some progressive failure in the major anti-trapezoidal teeth (see Fig. S2). In contrast, all of the samples with two orders of hierarchy demonstrate high levels of progressive failure as seen in Fig. 4d. In all cases, after an initial drop in load due to crack formation, the sample re-attains the same stiffness, with this pattern repeating until catastrophic failure occurs. This exhibits the flaw tolerance of the design, as the initial localized failures do not negatively impact overall performance. This also allows the parts to flex up to one millimeter from the initial crack (in 5°-5° configuration) before failure, offering 2.5 times greater flexibility than the base 5°- sample. Continuing to focus on these two samples, there is large drop in load occurring at the initial crack for the 5°-5° sample, occurring at nearly the same displacement as the 5°- sample occurred, inferring that major tooth fracture was responsible. Having the ability to control in which sequence teeth at different length scales fracture could provide unique design opportunities for these materials. In terms of ultimate flexural strength (UFS), the *N2* joints again out-performed the *N1* geometries by a significant margin (see Fig. 4c). For the samples having *N1* interlocking of 5°, a near linear increase in strength with *N2* interlocking angle is observed. For the 15° samples, the UFS does generally increase with *N2* angle, however the 25° samples demonstrates a much less significant dependence on geometry. In all cases, the addition of a second order of hierarchy increased strength. Notably, the dovetail sample with 15° of interlocking exhibited the best UFS of the non-hierarchical samples. Stiffness, on the other hand, showed few trends, with relatively good performance from the anti-trapezoidal samples. There is a slight increase in stiffness with *N1* interlocking for the anti-trapezoidal samples, and a slight decreasing trend for the hierarchal samples with *N2* interlocking equal to 15°, and 25° (see Fig. 4b). The highest and lowest stiffnesses were exhibited by samples having 15° of *N2* interlocking, exemplifying how sensitive stiffness is to geometric manipulation of the design. The 5°-25° sample was likely the least stiff due to the relatively narrow necks of the anti-trapezoids in this configuration. For the 5° set, a peak is apparent at 15°. The 5°-15° and 15°-35° samples exhibit the greatest stiffnesses, offering

25% increase over *N1* only. Looking across the sets discussed here, increasing interlocking angle to the extremes does appear to benefit stiffness in most cases. Across all hierarchical samples, energy dissipation correlated inversely with *N1* interlocking angle. This can be attributed to the 5°- samples having generally good flexibility without sacrificing strength or stiffness compared to the other sets. The best samples, 5°-5°, and 5°-35°, exhibited the most and second most energy dissipation of all tested. Consequently, lower *N1* interlocking angles are better suited to applications where high flexural toughness is desired. Further, these samples exhibit some of the best and worst flexural strength, indicating no correlation between strength and energy dissipation. The 5°-5° sample, exhibiting the extreme progressive failure and delayed failure, was an outlier among all samples. Of those tested, the samples with only one order of hierarchy exhibited significantly worse energy dissipation (see Fig. 4a). As cracks primarily formed along straight horizontal lines, propagating through the necks and extending to the edges, premature failure occurred. It could be of great use to investigate lower orders of *N1* interlocking in hierarchical samples in order to find the limits of the samples' ability to delay failure. Within *N1* groupings, we do not see much trend in terms of energy dissipation, although the 5°-35°, 15°-35°, and 25°-35° samples were the best or second best of their sets. Therefore, it can be concluded that there is a slight increase in energy dissipation with *N2* interlocking. The 15°-15°, and 25°-15° samples were also best or second best in their sets, inferring the 15° of *N2* interlocking offers good dissipation in certain hierarchical cases. The 15°-25°, and 25°-25° samples both exhibited very little progressive failure (1 or 2 cracks before catastrophic failure), making the 25°- samples some of the worst in terms of flaw tolerance. This parallels how the anti-trapezoidal samples failed, 25°- sample exclusive, with virtually no further extension after initial crack formation. In summation, samples having a variety of *N2* tooth shapes appeared to perform best, while those with similar corner and central teeth appear to underperform. This is likely due to the variance in neck width, resulting in sacrificial teeth dissipating energy early on. The anti-trapezoidal sample with 15° of interlocking demonstrated the best energy dissipation of the dovetail samples (along with its high strength), agreeing with other studies which found it to be the optimal angle for pullout without fracture [1-3].

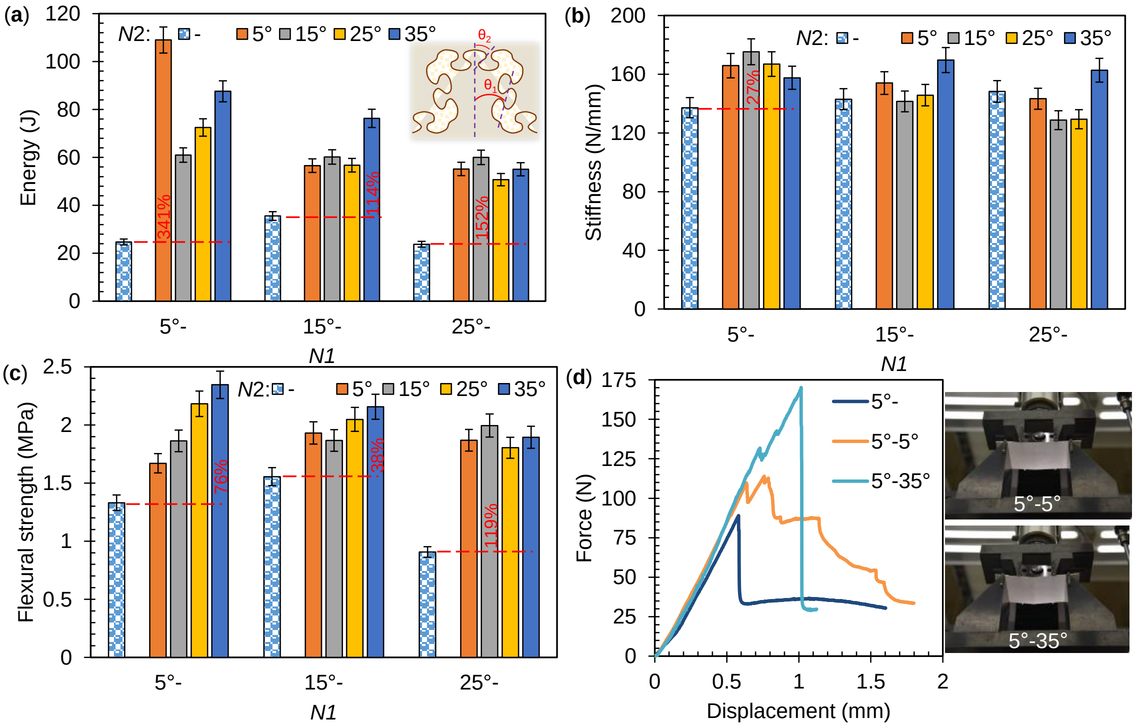

Figure 4: Bending properties of the ceramic sutures: (**a**) Energy absorption, (**b**) Stiffness, and (**c**) Flexural strength. (**d**) Force-displacement curves for where θ_2 (*N2*) = 5°, 35° and θ_1 (*N1*) = 5°.

2.3. Narrow Notch Side-loaded In-plane Fracture

Notched fracture tested samples exhibited rapid and instantaneous crack propagation compared to those tested in bending. This is attributed to the relatively fast displacement rate (5 mm/s) and crack-guiding effects of the notch. A baseline sample exhibiting one order of hierarchy was used to benchmark improvements toughness and energy absorption. Figure 5 present the fracture properties of ceramic suture including stiffness, maximum force, energy absorption, and fracture toughness. As visible in the DIC in Fig. 6, the more interlocked *N1* samples channeled strain concentration towards the corners of the teeth, which in the extreme cases, caused fracture to originate away from the notch (or for some cases the tooth pullout failure mode occurs). This is logical, as the length between the corner of the anti-trapezoid and the edge of the sample is less than the overall length of the notch. Interestingly, the 5°- sample absorbed the second most energy of all samples tested, although its fracture toughness was closer to the average. The anti-trapezoidal data demonstrates a clear inverse-correlation between *N1* interlocking angle and performance. As the least-interlocking sample provides the least resistance to vertical motion, the friction occurring at the interlocking interface is able to dissipate lots of energy. However, the motion/sliding at this interface is why the fracture toughness, which is dependent on slope of the load-displacement curve, is lower than some of the other samples. If the 15°- and 25°- were designed such that failure was guaranteed to occur at the notch, they would likely test better as well, as this factor had a significant impact on their overall performance. Looking to the hierarchical samples, the 15°-15° sample proved to be the toughest, demonstrating 60% greater fracture toughness than the baseline, with the second best energy absorption of the lot. Samples exhibiting 15° of *N2* interlocking generally performed well. The 5°-35° sample absorbed 140% more energy than the baseline (see Fig. 5b), offering the second best fracture toughness as well (aside from 5°- sample). As previously discussed, 15° has been validated as the optimal angle for frictional pullout without fracture [1-3], which corresponds to higher strength and energy absorption. In the side-loaded mode of fracture testing, the energy dissipated at these interlocked interfaces contributes to the toughness and energy absorption ability of the best samples. The 5°-35° sample, having performed well in multiple loading conditions, balances high and low interlocking in a more complex manner, dividing them among different hierarchy orders. With respect to notched fracture testing, this resulted in the highest fracture toughness, as the high interlocking of the *N2* teeth offered significant resistance to displacement, whereas the *N1* angle of 5° offers the widest base of the teeth and hence resistance to crack propagation. Considering the 5°-25° was a good performer, but the 15°-25°, 25°-25°, and 25°-35° samples less therefore, this theory is supported.

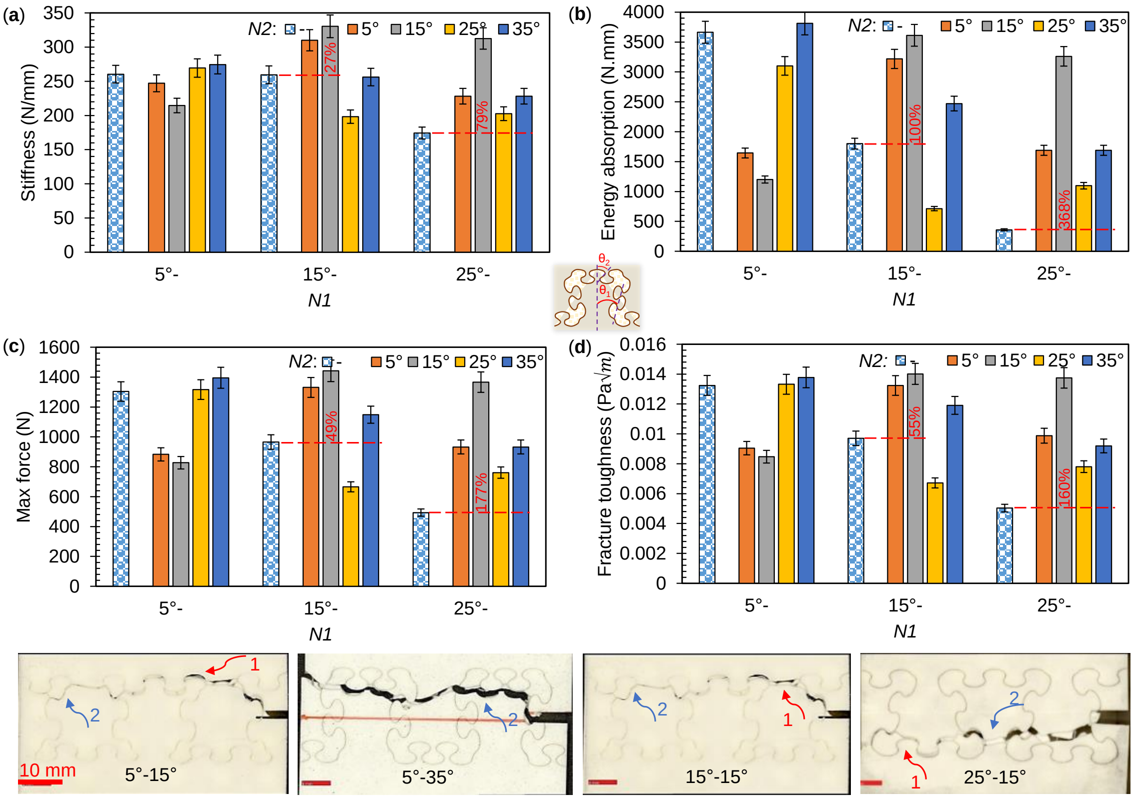

Figure 5: Fracture properties of the ceramic sutures: (**a**) Stiffness, (**b**) Energy absorption, (**c**) Max force, and (**d**) Fracture toughness for where θ_2 (*N2*) = 5°, 15°, 25°, or 35° and θ_1 (*N1*) = 5°, 15°, or 25° (Number 1: tooth pullout, and Number 2: tooth failure).

3. Discussion

Utilizing the developed digital manufacturing platform to precisely control the hierarchical interlocking of the architected sutures, a ceramic composite with significantly enhanced energy absorption and deformability has been developed. This automated manufacturing method facilitates the exploration of both extrinsic (behind crack tip) and intrinsic (ahead of crack tip) toughening mechanisms, each contributing to the energy absorption of the developed ceramic suture systems. These numerous mechanisms include plastic deformation in the adhesive interlayers, inter-tooth sliding (i.e., frictional energy dissipation), tooth pullout, delamination in adhesive interlayers and ceramic tiles, crack deflection, and ceramic tooth fracture.

Figures 8a-b illustrated the force-displacement curves for 5°-35° and 25°-35° ceramic sutures, in side-notched fracture. Both sutures deformed and failed via similar mechanisms (see Fig. 6b), however, the *N1* interlocking angle majorly contributed to performance. For the 5°-35° sutures, the force dropped at a higher maximum load and displacement compared to the 25°-35° ceramic suture. The force-displacement data reveals two obvious phases of deformation. In phase I, the force increases with displacement. Small drops may occur from the damage between the teeth, however the force continues to increase in this phase due to teeth interlocking. In this phase, no damage was observed in the adhesive interlayer, and no separation is visible in adjacent interlocking teeth. Phase II follows failure of the first tooth (as well as damage in in the adhesive interlayer) due to localized deformation and stress concentration near the tooth tip (reaching the peak load). A significant drop in force occurs considering the rest of the suture structure is unable to carry the load. In this phase, the suture is still able to carry a lesser load level up to the complete failure due to tooth failure or pull-out. Mixed failure mechanisms can be observed in the weak interface in phase II.

Figures 6c-e present the material performance with respect to toughness as a function of stiffness for all suture designs for tensile, bending, and fracture modes. The second order of hierarchy in the architected systems lead to reduced stiffness and high deformability when compared to those with the one order. This could be an advantageous for flexible protections (e.g. personnel protective equipment). It is illustrated in Fig. 6e how the sutured ceramics offer up to 358% improvements in energy absorption (fracture mode) in comparison to its baseline, which is significant for applications where energy must be dissipated.

Through precise geometry control afforded by the advanced manufacturing system, toughness, stiffness, and strength properties can be tuned for the desired for target engineering and armor applications. For instance, personnel protective equipment needs to be less stiff (to provide comfort). These properties are achieved by selecting a higher order hierarchy of and tuning *N2* interlocking angle without compromising the surface hardness and durability of the ceramic material. To further point out the tunability of overall mechanical behavior of the ceramic sutures, the best two sutures of each testing category are listed in Table 1. It is demonstrated that with energy dissipation in mind, the 15°-15° ceramic suture is the best candidate with high energy in the tensile and fracture modes, whereas the 5°-5° configuration is optimal in flexure.

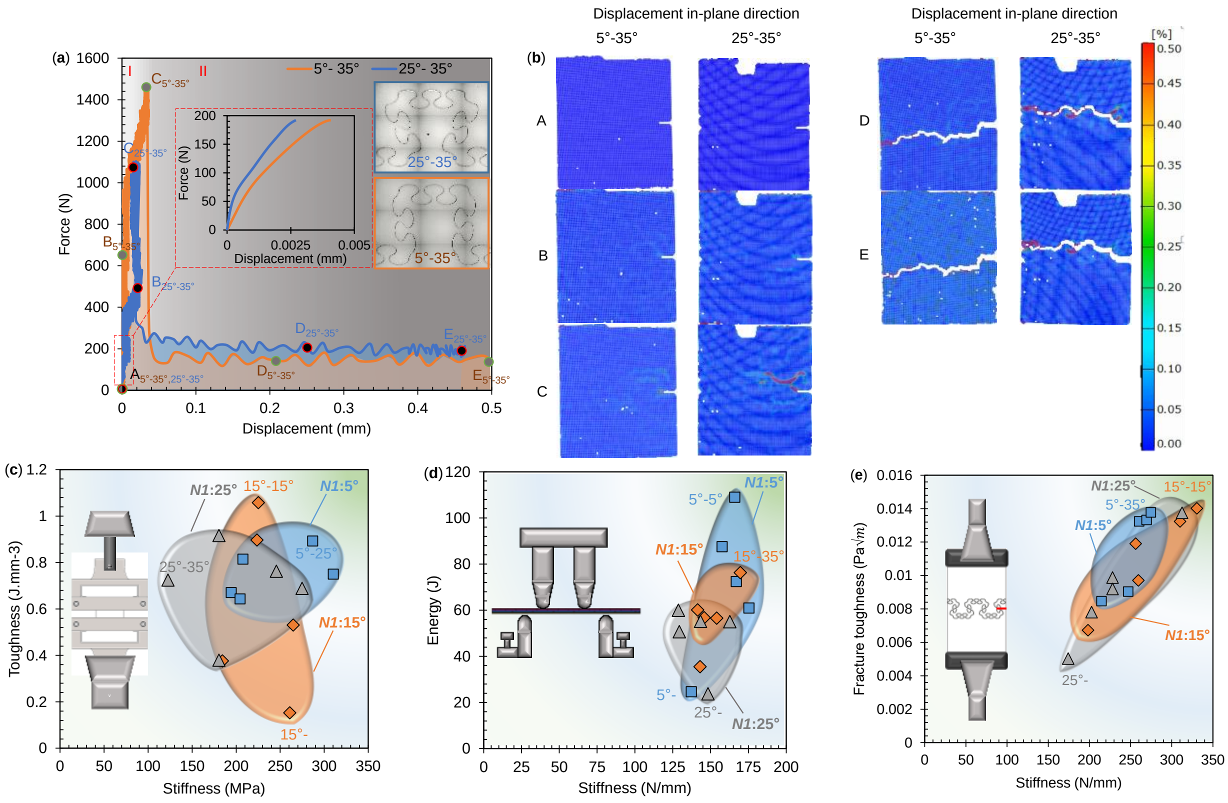

Figure 6: Fracture of 5°-35°, and 25°-35° ceramic sutures: (**a**) The force-displacement curves, (**b**) The in-plane displacement field at five stages of the loading. Comprehensive material performance of ceramic sutures in a toughness vs. stiffness plot: (**c**) Tensile, (**d**) Bending, and (**e**) Fracture.

Table 1: Best two ceramic sutures of each testing category.

Test / Term	Tensile		Bending		Fracture	
Energy absorption	15°-15°	25°-5°	5°-5°	5°-35°	5°-35°	5°-
Toughness	15°-15°	25°-5°			15°-15°	5°-25° 15°-25°
Strength	15°-15°	5°-25°	5°-35°	5°-25°		
Max force					15°-15°	5°-35°
Stiffness	5°-5°	25°-5°	5°-15°	15°-35°	15°-15°	25°-15° 5°-15°

4. Conclusions

Sutured structures are widespread in nature and have gained popularity in engineered bio-inspired applications. Due to their complexity, the sophisticated structures in nature that have resulted from years of evolution can only be replicated using advanced and intelligent manufacturing technologies. To study the effectiveness of bioinspired structural architectures in an engineered ceramic system, a manufacturing system was developed and a multi-modal mechanical study was performed to characterize the tensile, flexural, and fracture mechanics of hierarchical suture joints. Our near-net manufacturing system enables precise, defect free replication of bioinspired architectures with minimal material removal (to minimize reduction in stiffness). These engineered interfaces contribute to activate energy dissipation while ensuring geometric interlocking. In addition, the adhesive interlayer plays a significant role in toughness and stiffness tunability. Interlocking systems of two orders of hierarchy are explored, with anti-trapezoidal *N1* (:5°, 15°, 25°), as well as mixed-architecture *N1-N2* (*N1*: 5°, 15°, and 25° and *N2*: 5°, 15°, 25°, and 35°) ceramic sutures. The effects of the first and second orders of geometrical interlocking and loading modes on the deformation and failure mechanics of ceramic sutures were experimentally investigated by examining their force-displacement, stress-strain, and progressive failure responses. It is observed that the ceramic sutures with a second order of structural hierarchy offer substantial improvements in toughness by facilitating an enhanced interlocking, resulting in less brittle fractures. Comparing ceramic sutures with different geometrical hierarchical orders, the second order ceramic suture demonstrates both higher strength and deformability. For the first order ceramic sutures, the stiffness generally depends on the interface strength (i.e., tooth interlocking angle). On the contrary, for the second order ceramic sutures, the geometric interlocking and frictional interactions at the weak interfaces also contribute to the stiffness and strength of the structures. Different failure mechanisms due to the differences in the location of stress and strain were captured using DIC. Under load, it is observed that the maximum strain is extensively concentrated along the weak interfaces, leading to structural interlocking caused by geometric interference. The deformation of the ceramic suture increases up to the point where the teeth is either pulled out or fractured. The results infer that the toughness of ceramic sutures can be extensively enhanced by tuning the suture architecture, even when the neat substrate of the suture consists of an inherently brittle material. The developed design strategy opens up a new and large design space for architectured ceramics covering a broad range of engineering applications by tuning the geometric orientation (i.e., interlocking teeth), size (i.e., order of hierarchy), and tile-cut features (i.e., curvature) of trapezoidal morphologies in the ceramic suture system.

References

1. Rivera, J., et al., *Toughening mechanisms of the elytra of the diabolical ironclad beetle.* Nature, 2020. **586**(7830): p. 543-548.
2. Malik, I.A., M. Mirkhalaf, and F. Barthelat, *Bio-inspired "jigsaw"-like interlocking sutures: Modeling, optimization, 3D printing and testing.* Journal of the Mechanics and Physics of Solids, 2017. **102**: p. 224-238.
3. Mirkhalaf, M. and F. Barthelat, *Design, 3D printing and testing of architectured materials with bistable interlocks.* Extreme Mechanics Letters, 2017. **11**: p. 1-7.